Polymorphism in Thermoelectric As2Te3

Cédric Morin, Serena Corallini, Julie Carreaud, Jean-Baptiste Vaney, Gaëlle Delaizir, Jean-Claude Crivello, Elsa B. Lopes, Andrea Piarristeguy, Judith Monnier, Christophe Candolfi, et al.

▶ **To cite this version:**

Cédric Morin, Serena Corallini, Julie Carreaud, Jean-Baptiste Vaney, Gaëlle Delaizir, et al.. Polymorphism in Thermoelectric As2Te3. Inorganic Chemistry, 2015, 54 (20), pp.9936. 10.1021/acs.inorgchem.5b01676 . hal-01219302

HAL Id: hal-01219302
https://hal.science/hal-01219302

Submitted on 8 Mar 2023

HAL is a multi-disciplinary open access archive for the deposit and dissemination of scientific research documents, whether they are published or not. The documents may come from teaching and research institutions in France or abroad, or from public or private research centers.

L'archive ouverte pluridisciplinaire **HAL**, est destinée au dépôt et à la diffusion de documents scientifiques de niveau recherche, publiés ou non, émanant des établissements d'enseignement et de recherche français ou étrangers, des laboratoires publics ou privés.

Polymorphism in thermoelectric As_2Te_3

Cedric Morin[1], Serena Corallini[2], Julie Carreaud[3], Jean-Baptiste Vaney[4], Gaelle Delaizir[3], Jean-Claude Crivello[1], Elsa Branco Lopes[5], Andrea Piarristeguy[2], Judith Monnier[1], Christophe Candolfi[4], Vivian Nassif[6,7], Gabriel Julio Cuello[8], Annie Pradel[2], Antonio Pereira Goncalves[5], Bertrand Lenoir[4], Eric Alleno[1]*

[1] *Institut de Chimie et des Matériaux Paris Est (ICMPE), UMR 7182 CNRS-Université Paris-Est Créteil, Thiais, France*

[2] *Institut Charles Gerhardt (ICG), UMR 5253 CNRS-Université de Montpellier, France*

[3] *Science des Procédés Céramiques et de Traitements de Surface (SPCTS), UMR CNRS 7315-Université de Limoges, France*

k

[5] *C2TN, Instituto Superior Técnico, Universidade de Lisboa, Portugal*

[6] *Univ. Grenoble Alpes, Grenoble, France*

[7] *CNRS, Inst NEEL, Grenoble, France*

[8] *Institut Laue Langevin, Grenoble Cedex 9, France*

Abstract

Metastable β–As_2Te_3 (*R–3m*, *a* = 4.047 Å and *c* = 29.492 Å at 300 K) is isostructural to layered Bi_2Te_3 and is known for similarly displaying good thermoelectric properties around 400 K. Crystallizing glassy-As_2Te_3 leads to multiphase samples while β–As_2Te_3 could indeed be synthesized with good phase-purity (97 %) by melt quenching. As expected, β–As_2Te_3 reconstructively transforms into stable α-As_2Te_3 (*C2/m*, *a* = 14.337 Å, *b* = 4.015 Å, *c* = 9.887 Å and β = 95.06°) at 480 K. This $\beta \rightarrow \alpha$ transformation can be seen as the displacement of part of the As atoms from their As_2Te_3 layers into the van der Waals bonding interspace. Upon cooling, β–As_2Te_3 displacively transforms in two steps below T_{S1} = 205 – 210 K and T_{S2} = 193 – 197 K into a new β' –As_2Te_3 allotrope. These reversible and first-order phase transitions give rise to anomalies in the resistance and in the calorimetry measurements. The new monoclinic β' –As_2Te_3 crystal structure (*P2₁/m*, *a* = 6.982 Å, *b* = 16.187 Å, *c* = 10.232 Å, β = 103.46° at 20 K) was solved from Rietveld refinements of X–ray and neutron powder patterns collected at low temperatures. These analyses showed that the distortion undergone by β–As_2Te_3 is accompanied by a 4–fold modulation along its *b*–axis. In agreement with our experimental results, electronic structure calculations indicate that all three structures are semiconducting with the α–phase being the most stable one and the β'–phase being more stable than the β–phase. These calculations also confirm the occurrence of a van der Waals interspace between covalently bonded As_2Te_3 layers in all three structures.

Introduction

Chalcogenides compounds with generic formula A_2X_3 (A = Sb, Bi and X = S, Se, Te) and rhombohedral symmetry ($R\bar{3}m$) have been investigated for nearly six decades for their thermoelectric properties [1-3]. When properly optimized, these materials display a dimensionless thermoelectric figure of merit (ZT) close to unity and, to date, still remain the most efficient thermoelectric materials for room-temperature applications. However, it is not until recently that good thermoelectric properties were unveiled in isostructural β–As_2Te_3 which displays a peak ZT of 0.65 at 423 K upon Sn doping [4]. This late discovery is related to the fact that rhombohedral β–As_2Te_3 is a metastable form of As_2Te_3 [5], which was known to exist under two other allotropic forms: the stable crystalline α–As_2Te_3 phase (monoclinic $C2/m$) [6,7] and a metastable glassy As_2Te_3 form [8]. Increasing the cooling rate favors the synthesis of the metastable phases: slow cooling, melt-quenching and twin-roller quenching indeed lead to α–As_2Te_3, β–As_2Te_3 and glassy–As_2Te_3, respectively. Upon heating, glassy–As_2Te_3 and β–As_2Te_3 irreversibly transform into α–As_2Te_3 [9].

A precise knowledge of the structural and electronic properties of these phases is not only important for thermoelectricity but also for both other applications and fundamental reasons. The A_2X_3 (A = Sb, Bi and X = Se, Te) compounds are nowadays known as three-dimensional topological insulators [10-13]: they are bulk insulators but display "topologically protected" gapless surface states which can non-dissipatively carry spin current [14]. β–As_2Te_3 is indeed expected to become a topological insulator under high pressure [15]. It is also well known that arsenic and tellurium are common elements in several multicomponent amorphous/glass-ceramics systems which show electrical threshold and memory switching properties [16 17]. Crystallization induced in these materials by an electric field, by heating, or by radiation yields As_2Te_3 crystallites [8,18]. More recently, layered chalcogenides have received attention, due to the possibility to intercalate positive ions [19] or as components of infrared optical systems [20].

Herein, we provide a detailed structural study of α–As_2Te_3 and β–As_2Te_3. Besides confirming the main crystallographic features of the former, our reinvestigation of the latter yields a more precise description of its crystal structure. In addition, our results evidence a reversible first-order, two-step structural transition at T_{S1} = 205 – 210 K and T_{S2} = 193 – 197 K. Across this transition, the rhombohedral symmetry of β–As_2Te_3 ($R\bar{3}m$) changes into the monoclinic β' –As_2Te_3 (space group $P2_1/m$). This transition leaves clear signatures in the low-temperature resistance and thermodynamic properties, which shows a weak hysteretic behavior between cooling and heating cycles.

These experimental results are complemented by electronic structure calculation performed in the frame of the density functional theory (DFT). This part provides a relative stability comparison between the α, β, and β' phases and a chemical bonding details for these phases.

Experimental and calculation details

Two methods were implemented to synthesize the β–As_2Te_3 crystalline phase. The first one involves glassy As_2Te_3 in an intermediate stage. This glass was synthesized by melting at 923 K a stoichiometric composition of As (Goodfellow, 99.99 %) and Te ($5N^+$, 99.999 %) in a quartz tube sealed under secondary vacuum. After being held at this temperature for 2 h, the sample-filled ampoule was rapidly quenched in a "salt + ice + water" bath. The obtained materials were then crushed in small pieces and re-melted using the twin roller quenching technique described in details by Pradel *et al.* [21]. In the second stage, glassy-As_2Te_3 was hand-ground and sintered at 403 K and 413 K under an uniaxial pressure of 50 MPa in a Spark Plasma Sintering (SPS) system (Fuji Electronic DR SINTER Lab 515S). The second method for β-As_2Te_3 synthesis is a direct melting at 923 K of stoichiometric quantities of As and Te in a quartz tube sealed under vacuum. This tube was heated up to 923 K at a rate of 10 K·min^{-1}, dwelt at this temperature for 2 hours and quenched into water. The resulting ingots were finally hand-ground to a micron-sized powder. A part of the powder was uniaxially pressed at room temperature under 750 MPa for C_p measurements.

The crystal structure and phase composition of the samples were determined at room temperature by powder X-ray diffraction (PXRD) using a Bruker D8 diffractometer (Cu–Kα radiation) equipped with a Vantec 1D detector. The microstructure was investigated on powdered samples by scanning electron microscopy (SEM) using a Jeol 7400F Field Emission Scanning Electron Microscope.

Electrical resistivity measurements were performed on a sub-millimetric particle of powder in the 25–300 K temperature range in a previously described cell [22], attached to the cold stage of a closed cycle cryostat. The resistivity was measured by a four-probe method using a lock-in amplifier (SRS Model SR830 DS) at a low frequency of 77 Hz.

The thermodynamic behavior of the samples was studied between 150 K and 573 K by differential scanning calorimetry (DSC) using a commercial instrument (TA Q100). Data were collected on both cooling and heating at a rate of 10 K·min^{-1}. Specific heat measurements were also performed using a Physical Properties Measurement System (Quantum Design) between 2 K and 300 K using a conventional relaxation method. A small sample of approximately 20 mg was glued on

the sample holder using a tiny amount of Apiezon N grease. Temperature was varied at a quasi-static rate.

To identify the low-temperature crystal structure, PXRD measurements were carried out on several β–As_2Te_3 samples between 20 K and 300 K using a Panalytical Empyrean diffractometer operating in Bragg-Brentano geometry with Cu–Kα radiation equipped with a pixel detector and an Oxford cryostat PheniX (He cryostat). These low-temperature structural investigations were complemented by neutron powder diffraction (NPD) experiments performed using the D1B instrument at the Institut Laue-Langevin (Grenoble, France). The instrument is a two-axis diffractometer having a banana-like Position Sensitive Detector composed by ^{3}He/CF4 1280 cells with a step of 0.1° in 2θ. The samples were placed in non-sealed cylindrical vanadium containers with an inner diameter of 7.6 mm, under Helium exchange gas. The standard ILL cryofurnace and its control system allowed performing cooling ramps at a rate of about 3.8 K·min^{-1} from 300 K down to 20 K, with annealing steps of about 1-2 h at 300 K, 190 K, 120 K and 20 K. The incident neutron wavelength was selected by using a pyrolytic graphite monochromator (plane 002). The exact values of the wavelength (2.5302 Å) and the zero-angle correction (0.006356) were determined by means of an independent measurement using a $Na_2Ca_3Al_2F_{14}$ powder sample as a standard. Rietveld refinements on X-ray and neutron powder diffraction patterns were carried out using the FULLPROF program [23]. The PXRD at 300 K, the electrical resistance $R(T)$, the calorimetry measurements and the low temperature PXRD and NPD were performed on separate β–As_2Te_3 batches: the good agreement between the various techniques of investigation points towards a weak dependence of the transition temperature on the sample batch.

Based on the density functional theory (DFT), electronic structure calculations have been performed using the projector augmented wave method (PAW) [24], implemented in the Vienna Ab initio Simulation Package (VASP) code [25], [26] with the generalized gradient approximation (GGA) by the use of Perdew–Burke–Ernzerhof (PBE) exchange-correlation functional [27]. The cut-off energy for the pseudo-potentials was set to 800 eV, and a dense grid of k-points in the irreducible wedge of the Brillouin zone was considered. Within a non-relativistic description, the electron spin-orbit coupling is neglected. Both the lattice parameters and the internal atomic coordinates were fully relaxed so that the convergence of Hellmann-Feynman forces was better than 0.1 meV/Å. Phonon calculations have been performed using the harmonic approximation (HA) from the supercell approach with the finite displacement method [29] using the Phonopy code [30] (cells with 60 to 80 atoms, see details in Table 7). The zero-point energies (ZPE) are obtained from the sum over all phonon modes (k-points and branches). The charge transfers have been computed using Bader's topological analysis [31].

Results and discussion

Synthesis of the β–As_2Te_3 phase

a) Crystallization of β–As_2Te_3 in glassy-As_2Te_3 under pressure

β–As_2Te_3 could not be obtained by crystallization from glassy As_2Te_3 under ambient pressure. Upon heating the glass, crystallization of AsTe was initially observed, followed by crystallization of α–As_2Te_3 (supplementary materials). Early studies have reported β–As_2Te_3 as a high-pressure phase obtained from a pressure-induced structural transition of the monoclinic variant α–As_2Te_3 near 7 GPa [32]. In order to force the crystallization of β–As_2Te_3, a moderate uniaxial pressure (50 MPa) was applied in the course of the temperature rise in the SPS system. Fig.1 shows the XRD patterns of two glassy samples sintered at 403 K and 423 K. The pattern of the former sample obviously corresponds to a glass-ceramic, *i.e.* crystallized particles embedded in a glassy matrix. Similarly to what is observed under ambient pressure, the first crystalline phase that appears inside the glass is not β–As_2Te_3 but cubic AsTe [33] [34]. Even if the expected β–As_2Te_3 phase is eventually obtained through a higher sintering temperature (423 K), the sample is not pure and a mixture of AsTe and glass remains present.

b) Direct synthesis of β-As_2Te_3 by melt-quenching

Previous experimental work has suggested that melt-quenching procedures are sufficient to directly synthesize bulk samples of β–As_2Te_3 [5]. This "slow" quenching process – in comparison to twin roller quenching - was implemented as described in the experimental part. The PXRD pattern, shown in Fig.2, confirms that β–As_2Te_3 crystallizes in the Bi_2Te_3-structure type with space group *R*–3*m* and lattice parameters *a* = 4.047(1) Å and *c* = 29.498(1) Å (hexagonal description). These values are close to those found in literature, *a* = 4.06 Å and *c* = 29.59 Å [5]. According to the Rietveld refinement, the main phase is β-As_2Te_3 (97_{mass} %) accompanied by a small fraction of AsTe (main peak near 31.0°) and arselonith-As_2O_3 (main peak near 13.8°) as secondary phases (both ~ 1_{mass} %). Based on the intensity of the enthalpy peak ascribed to the crystallization of AsTe in the sample, a glass residual fraction can be evaluatd to about 1_{mass} % (more details in supplementary materials).

A SEM image (Fig.3) taken on the surface of a partially broken grain of powder shows in several places a uniformly layered microstructure, consistent with the layered crystal structure of β–As_2Te_3.

Polymorphism of β-As_2Te_3 with temperature

a) Room temperature structure

We accurately re-determined the room-temperature crystal structure of β–As_2Te_3 to perform a detailed comparison with its high- and low-temperature allotropic forms. The XRD pattern (R_B = 4.3 % and R_{wp} = 6.8 %) at 300 K is displayed in Fig.2. A preferred orientation of the crystallites – platelets habit perpendicular to (0 0 1) - resulted in a very shallow renormalization of the relative intensities of the Bragg peaks. Structural parameters such as the atomic coordinates and isotropic displacement parameters were refined while the site occupation factors were held fixed at 1, corresponding to full occupancy. All these structural parameters are listed in Table 1.

This well-known crystal structure is displayed in Fig.4. It is built by stacking perpendicular to its *c*-axis planar As_2Te_3 layers linked by van der Waals bonds [35]. These bonds can easily be broken [36] and give rise to cleavage or exfoliation. The Te1 atoms are covalently coordinated by 6 next-nearest As atoms and the coordination polyhedron is a slightly distorted octahedron with its axis As-Te1-As being non perpendicular to the square plane Te1-As-As-As-As (95.7°). The As atoms are covalently coordinated to 3 Te1 atoms and 3 Te2 atoms and their coordination polyhedron is an irregular octahedron: the As-Te1-Te1-Te2-Te2 square is non planar and the opposite Te2-As and As-Te1 bonds are neither collinear (174.4°) nor strictly perpendicular (91.6° or 92.3°) to the square. Te2 atoms are coordinated to 3 As atoms by covalent bonding and to 3 other Te2 atoms by van der Waals bonding forming a trigonal antiprism.

Selected distances and angles for β–As_2Te_3 are reported in Table 2 and compared to those of Sb_2Te_3[11], Bi_2Te_3 [10] and β–As_2Te_3 [9]. The length of the covalent bonds *X* - Te1 and *X* - Te2 (*X* = As, Sb or Bi) consistently increases in accordance with the atomic radii of *X*, which are 1.15, 1.45 and 1.60 Å, respectively. The As - Te1 bond length obtained in this work is shorter than that reported by Shu *et al.* [5] (3.02 instead of 3.13 Å), whereas the present As - Te2 bond length is longer (2.81 instead of 2.75 Å). Dissymmetry of the distorted-octahedral bonding can be estimated by the ratio between the shorter (*X* - Te2) and the longer (*X* - Te1) covalent bond. The ratio reported by Shu *et al.* [5] (0.876) would indicate a high dissymmetry for the $AsTe_6$ octahedron. Yet, the present value of 0.930 points towards a more symmetric As - Te octahedron, in agreement with the ratios observed in Sb_2Te_3 and Bi_2Te_3 (0.939 and 0.941, respectively). The values of the Te1 - *X* - Te1, Te2 - *X* - Te2 and *X* - Te1 - *X* angles are also different from those obtained by Shu *et al.* but in excellent agreement with those found in Sb_2Te_3 and Bi_2Te_3.

Unlike the *X* - Te bond lengths, the Te2 - Te2 distance does not strictly vary in accordance with the atomic radii of *X*: these van der Waals bond lengths are longer in β–As_2Te_3 (both in this work and

in Shu *et al.*[5]) than the van der Waals bonds in Sb_2Te_3 and Bi_2Te_3. This effect is accompanied by an increase in the Te2-Te2-Te2 angle on going from As to Sb and eventually to Bi. The Te2 - Te2 interlayer distance (d_i), which can be defined as the distance along the *c*-axis between two contiguous Te2 layers and given by the expression, $d_i = (\mathrm{Te}2 - \mathrm{Te}2)\sqrt{1 - \frac{4}{3}\sin^2(\mathrm{Te}2 - \mathrm{Te}2 - \mathrm{Te}2)}$, decreases in good agreement with the atomic radii of *X*. From this, a stronger anisotropy of the in-plane and out-of-plane transport properties is expected when *X* changes from Bi to Sb and eventually to As.

b) High temperature transformation to α–As_2Te_3

Upon heating, the DSC thermogram (Fig.5) of the as-synthesized β–As_2Te_3 sample is characterized by two exothermic peaks. The first peak of low amplitude starts at 415 K and continues up to 455 K while the second peak extends from 460 K to 545 K (main onset at 480 K). The former is spurious and likely arises from the crystallization of a small amount of residual vitreous phase formed during the quenching process of the sample. The latter, however, delineates the phase transformation of β–As_2Te_3 into the stable α–As_2Te_3 phase. This irreversible phase transition has been previously observed by Toscani [9], who derived a transformation enthalpy of 9.6 J/g. This value is indeed very close to the measured value of 8.7 J/g. The X-ray thermodiffraction (see inset Fig.5) confirms that the phase transformation of β–As_2Te_3 into the stable phase α–As_2Te_3 develops between 453 K and 473 K, in agreement with the DSC data.

The crystal structure of α–As_2Te_3 was verified by Rietveld refinement of its PXRD pattern measured at 300 K. All the structural parameters were refined except the site occupation factors, which were kept fixed at full occupancy. Fig.6 shows the good quality of the fit and Table 3 lists the derived structural parameters. The lattice cell parameters of α–As_2Te_3 are very close to those found in literature. Indeed, Stergiou *et al.* [7] reported 14.357 Å, 4.020 Å, 9.899 Å and 95.11° while the present refinements yield 14.337(1) Å, 4.015(1) Å, 9.887(1) Å, 95.06(1)° for *a*, *b*, *c* and β angle, respectively.

A sketch of the α–As_2Te_3 structure is displayed in Fig.7 and Table 4 gathers all distances of interest. Similarly to β–As_2Te_3, this structure is also built by piling along its *a*–axis As_2Te_3 layers linked by van der Waals bonds. However, these layers are no longer planar but rather zig-zag-like. Compared to β–As_2Te_3, no Te atom and only half of the As atoms are octahedrally coordinated. The Te1 and Te3 sites are covalently coordinated to 3 As atoms, whereas Te2 is covalently coordinated to 5 As atoms forming a square-based pyramid (Fig.7b). Te2 is slightly above the square-base As2-As1-

As1-As2 (As2-Te2-As1 = 173°). As1 possesses similar square-based pyramid coordination with 5 Te. Again, As1 is slightly above the square-base of the pyramid (Te2-As1-Te3 = 177°). As2 is octahedrally coordinated by 6 Te atoms. The bond lengths in β–As_2Te_3 and in α–As_2Te_3 are quite similar. Indeed, the length of the covalent As-Te bonds in α–As_2Te_3 (from 2.65-3.25 Å) is nearly equivalent to the covalent bonds in β–As_2Te_3 (2.81-3.02 Å). Furthermore, the van der Waals Te – Te bond lengths in α–As_2Te_3 (ranging between 3.68 Å and 3.76 Å) are close to the distance measured in β–As_2Te_3 (3.73 Å). However, the α–As_2Te_3 structure shows a new van der Waals type bond: As1 – As1. Its distance is slightly shorter than the Te - Te bonds (3.54 Å). The difference between these covalent bond distances and those reported in literature [7] are less than 0.02 Å, which corresponds to a relative departure of less than 0.6 %.

The transition from β–As_2Te_3 to α-As_2Te_3 is a reconstructive transformation with new bonds created during the transformation, in line with the sizable enthalpy. Fig. 8 shows in details the structural relationship between the two allotropes more clearly. Keeping the Te atoms in their layers but allowing for relaxations, moving two over six As atoms from their layers into the van der Waals interspace and covalently bonding them to the nearby Te atoms indeed transforms β–As_2Te_3 into α-As_2Te_3. By doing this way, the conditions of periodicity, minimum number and minimum distance of atomic displacements are fulfilled. However, it should be kept in mind that although this scheme could represent the chemical reaction path, neither an experiment nor a theory currently supports this idea and hence, this process should only be seen as a structural construction.

c) Low-temperature thermodynamic and transport properties of β–As_2Te_3

The electrical resistance as a function of the temperature is shown in Fig.9a. Upon cooling to 20 K, $R(T)$ decreases with temperature from 300 to 200 K where a steplike increase is observed. The $-dR/dT$ data (Fig.9b) show that the jump extends between 195 K and 180 K with onset at 195 K and maximum at 191 K. Such anomaly in $R(T)$ suggests a structural phase transition.

In order to further characterize the thermodynamic properties of the phase transition, specific heat data $C_p(T)$ have been measured in the vicinity of the transition by cooling down to 2 K a β–As_2Te_3 sample (Fig.10a). The transition shows up as a pronounced hump between 160 K and 210 K, peaking at 187 K. The results of the specific heat measurements were complemented by DSC experiments shown in Fig.10.b. Upon cooling, an exothermic peak sets in at 185 K while an equivalent endothermic peak is observed with a 4 K hysteresis at 189 K in the heating curve, indicative of the reversibility of the transition and its first order nature. A closer examination of the cooling data leads to fitting in a crude fashion two symmetric peaks (Lorentzian) with characteristic

temperatures of $T_{S1}^{DSC} = 192\,K$ and $T_{S2}^{DSC} = 189\,K$ for the less and the most intense peak, respectively. As we shall see below by following the distortion parameters related to the lattice parameters, these two peaks are suggestive of a two-step transition. $T_{S1}^{DSC} = 192\,K$ is in agreement with that inferred by R(T) measurements and slightly shifted from that inferred from specific heat data ($T_{S1} = 205 - 210\,K$). This most probably arises from differing sample batches and/or differing cooling rates. The weak enthalpy of transformation derived from these data (~1 $J \cdot g^{-1} \cdot K^{-1}$) is consistent with that derived from specific heat (~0.6$\cdot J \cdot g^{-1} \cdot K^{-1}$) and provides an experimental clue that the transition induces minimal transformation of β–As_2Te_3.

d) A new low-temperature structure: β'–As_2Te_3

Given the low-temperature transport and thermodynamic behavior of β–As_2Te_3, X-ray (supplementary materials S3) and neutron diffraction experiments (supplementary materials S4) as a function of temperature were carried out between 20 K and 300 K to study the nature of the transition and the possibility of a new low-temperature crystal structure. A rapid examination of the neutron diffraction patterns as a function of temperature, shown in the inset of Fig. 11, led to the conclusion that only one structural transition from β–As_2Te_3 to an unknown structure occurs around 200 K, close to the temperature onset seen in transport and calorimetric experiments.

The PXRD pattern recorded at 20 K on β–As_2Te_3 (Fig. 12) only slightly differs from that measured at 300 K. However, at 2θ = 30°, 2θ = 42° and 2θ = 62° (see inset of Fig. 12), the (0 1 5), the (0 1 11) and the (0 2 10) reflections split into two lines. Thus, we considered that the low-temperature unit cell corresponds to a distorted hexagonal unit cell of lower symmetry, which according to group-subgroup relationships, could be monoclinic with space group *C*2/*m*. A preliminary attempt to refine the 20 K pattern with the α–As_2Te_3 structure (*C*2/*m*) did not provide an accurate description of the PXRD data and the unit cell of β–As_2Te_3 was rather used as a starting point for indexing. Following Mukai et al. [37], we transformed its hexagonal description into a monoclinic description using the following matrix relationship between the two settings:

$$\left(\vec{a}\,\vec{b}\,\vec{c}\right)_m = \begin{pmatrix} 2 & 0 & 2/3 \\ 1 & 1 & 1/3 \\ 0 & 0 & 1/3 \end{pmatrix} \left(\vec{a}\,\vec{b}\,\vec{c}\right)_h$$

where *m* and *h* represent the monoclinic and the hexagonal settings, respectively. Monoclinic lattice parameters a_m, b_m, c_m and β_m are thus related to the hexagonal lattice parameters a_h and c_h as follows:

$$a_m = a_h\sqrt{3} \quad (1)$$
$$b_m = b_h = a_h \quad (2)$$
$$\beta_m = 180° - \tan^{-1}\left(\frac{c_h}{a_h\sqrt{3}}\right) \quad (3)$$
$$c_m = \frac{c_h}{3\sin\beta_m} \quad (4)$$

We initially indexed the 20 K PXRD data with this base-centered monoclinic unit cell with a = 6.984 Å, b = 4.049 Å, c = 10.238 Å, β = 103.45°. However, several reflections in the 20 K NPD, with a faint but varying intensity with temperature, remained unindexed (Fig. 11). Thanks to an automatic indexing program (TREOR [38]), we found that a primitive monoclinic unit cell with a = 6.982(1) Å, b = 16.187(1) Å, c = 10.232(1) Å, β = 103.47(1)° could index both the 20 K NPD and PXRD patterns. This final unit cell is thus not only a monoclinic distortion of the 300 K hexagonal unit cell but also a superstructure with a $b_m = 4a_h$ modulation. In both patterns, additional reflections with temperature independent intensities were ascribed to AsTe (0.5 % mass) and arselonith As_2O_3 (0.1% mass). In NPD patterns, As_2O_5 (0.1 % mass) could also be detected (Fig. 11) while very weak peaks remained unindexed. Claudetite-As_2O_3 was envisaged as an extra secondary phase to index these remaining peaks but its occurrence could not be firmly established. Systematic extinctions ((0*k*0), *k* odd) led to the choice of centro-symetric $P2_1/m$ as the space group.

The motif of β–As_2Te_3 was also transformed into the monoclinic description to obtain a starting point for the Rietveld refinement of the 20 K NPD pattern, followed by the refinement of the 20 K X–ray data. Again, the atomic coordinates and isotropic displacement parameters were refined while the site occupation factors were kept fixed at full occupancy. Fig.12 and Fig.13, respectively, show the results of the X–ray and neutron Rietveld analyses highlighting their good agreements with experiments (R_B = 9.5 %, R_{wp} = 2.4 % and R_B = 1.7 %, R_{wp} = 4.2 %, respectively) with the experiments. Table 5 reports the atomic positions while Fig.15 shows a sketch of this new structure hereafter called β' – As_2Te_3. The β -> β' transition unveiled by the transport properties measurements is hence a structural transition with a reduction of symmetry from space group *R*-3*m* to $P2_1/m$ accompanied by a weak modulation along the b_m–axis of the atomic positions parallel and perpendicular to this axis. This transformation is a displacive transition since it does not add or remove any chemical bonds and only modifies bond lengths and angles (see Fig.15). The atomic sites in β'–As_2Te_3 are gathered in

Table 5 according to their parentage with those in β–As_2Te_3 : {As1 – As5} = As parentage, {Te1 – Te3} = Te1 parentage and {Te4 – Te8} = Te2 parentage. The Te2 parentage, Te1 parentage and As parentage sites do not form planar layers anymore and their coordination polyhedra are distorted but conserved, e.g. As_3Te_3 antiprism, As_6 and Te_6 octahedra, respectively. Because of the numerous different atomic distances in β'–As_2Te_3, only averages and ranges were listed in Table 6 according to their site parentage to β–As_2Te_3. The average As parentage – Te1 parentage bond length is conserved while the average As parentage – Te2 parentage and Te2 parentage – Te2 parentage bond lengths increase only by few hundredths of angstrom. The strong intensity of the distortions can be better evaluated by the ranges of these bond lengths: ±0.35, ±0.2 and ±0.25 Å for the As parentage - Te1 parentage, As parentage - Te2 parentage and Te2 parentage - Te2 parentage, respectively. These ranges of distances are nonetheless in agreement with those found in α–As_2Te_3 (see table 4). The average volume per atom in β' –As_2Te_3 at 20 K is 28.3 $Å^3$ while it corresponds to 27.9 $Å^3$ in β–As_2Te_3 at 300 K: upon cooling, the phase transition counteracts the thermal contraction, thereby expanding the atomic volume and leading to a less dense structure at low temperature.

e) Temperature dependence of the neutron intensities and distortion parameters

The β–As_2Te_3 -> β'–As_2Te_3 transition can be structurally monitored as a function of temperature by the change in the intensity of low-angle reflections in the neutron diffraction data which appears upon cooling. They are displayed in Fig.15 and at least one of them at $2\theta = 35.5°$ can be observed below 201 – 205 K. Given the signal-to-noise ratio in these patterns, distortion parameters are more adequate quantities to finely monitor the transition with temperature. Their definition arises from the transformation relationships (see previous part) between the hexagonal and monoclinic unit cells:

$$\Delta a = \sqrt{3}\, b_m / 4 - a_m \qquad (5)$$

$$\Delta\beta = \beta_m - \beta_h = \beta_m - \left[180° - \tan^{-1}\left(\frac{3 c_m \sin\beta_m}{a_m} \right) \right] \qquad (6)$$

Δa and $\Delta\beta$, which are displayed in Fig.16, reflect the monoclinic distortion in the basal (***a***, ***b***) plane and out of this plane, respectively. Both parameters slightly differ from zero (more details in supplementary materials about this point) in the rhombohedral phase but their nearly constant value sets a well-defined baseline that allows for a fine detection of the transition. The non monotonous variations of Δa and $\Delta\beta$ at the transition are characteristic of a two-step transition. Upon cooling, at T_{S1} = 205 – 209 K Δa and $\Delta\beta$ decreases and increases respectively, starting from their rhombohedral

value. At T_{S2} = 193 – 197 K, Δa and $\Delta\beta$ increases and decreases respectively. T_{s1} is in good agreement with the onset temperatures derived from *R(T)* and $C_p(T)$ data (T_{S1} = 205 – 210 K) while T_{s2} corresponds to the more intense peak in the DSC data (onset at $T_{S2}^{DSC} = 192\,K$). Of note, because both parameters reach a steady state regime with expected positive values, T_{S2} should correspond to the rhombohedral-to-monoclinic distortion while T_{S1} should arise from the 4-fold modulation of the b_h-axis (// b_m-axis), in agreement with the appearance of the low-angle neutron reflections below 201 – 205 K (Fig.16). Displacive transitions are usually related to soft phonon modes with frequencies going to zero upon temperature variations [39]. It can be conjectured that this two-steps transition in β–As_2Te_3 could arise from two separate phonon mode(s), which simply soften at separate temperatures.

DFT calculations

a) Crystal structure stability

The DFT-calculated lattice parameters of the three polymorphic As_2Te_3 phases (α, β, β') are slightly larger (less than 3 %) than the experimental ones (Table 7). This effect is explained by the choice of the GGA exchange-correlation function, which is known to overestimate cell volume. Comparison of the equilibrium volume by atom in the three structures indicates that the smaller and larger values are obtained for the β–As_2Te_3 and α–As_2Te_3 phases, respectively (about 30 Å^3/atom). The intermediate volume is found for β'–As_2Te_3, as expected from the experimental measurements (the β'–phase can be seen as an expansion of the β–phase at low temperatures). More details on the electronic structure, accompanied by transport measurement, will be provided in a forthcoming paper.

After the internal parameters relaxation (resulting illustration is shown in Fig.17), the zigzag layer in α–As_2Te_3 phase and the interlayer between Te atoms of the β–As_2Te_3 remain unchanged (distance of 3.85 Å for this later). As for the β'–phase, starting with the initial parameters from the experimental description in $P2_1/m$ (11) space group, its relaxation converges to the loss of the modulation along the b_m–axis. In this way, relaxation leads to the substructure description in space group $C2/m$ (12) with a_h = ¼ b_m in agreement with our first Rietveld analyses of the PXRD data at 20 K. A proposition of simplification of the β'–phase description in $C2/m$ consists in merging of all As atoms in one equivalent site: the 4*i* (*x* = 0.394, *z* = 0.182), and the Te atoms in two sites : 2*a* and 4*i* (*x* = 0.220, *z* = 0.661). In this way, the DFT calculation at 0 K suggests a higher symmetry compared with the analyses of the NPD data at 20 K.

The heat of formation of As_2Te_3, calculated in all φ symmetries, is given by the difference of total energies: $\Delta_f H = E^{\varphi}(As_2Te_3) - 2\times E^{A7}(As) - 3\times E^{A8}(Te)$, where *A*7 and *A*8 are the strukturbericht notation of the stable structure of pure As and Te, respectively. As expected from our experimental findings, the α–phase is the most stable structure while the β'–phase is more stable than the β–phase. Since the β'–phase calculated in $P2_1/m$ relaxes to the $C2/m$ space group, their $\Delta_f H$ are equivalent. The ZPE corrected heats of formation, $\Delta_f H^{cor}$, are also indicated in Table 7, and present similar trends that the gross $\Delta_f H$ values. Each heat of formation does not exceed -2 kJ/mol·at and is close in energy, which suggests that the compound formation is not strongly exothermic and that phase-pure As_2Te_3 could be difficult to synthesize.

b) Chemical bonds

A basic analysis of the chemical bonds could be done thanks to the electronic localization function (ELF) representation (Fig.17.). This function takes values between 0 (no probability) to 1 (perfect localization) of the valence electrons, 0.5 indicating electron gas-like probability [40]. Plans have been chosen with 2 Te atoms in the interlayer of each polymorphic phase. This choice suggests that an electron-free zone exists between the as-mentioned interlayer and justifiy the “van der Waals bonds” appellation earlier in the paper between the Te atom plans for all As_2Te_3 forms and between As atoms for α-As_2Te_3. Moreover, the no-null ELF region (> 0.25) explains the interaction nature between As and Te by a sharing of valence electrons. Table 8 gives the electron charge transfer from As to Te. Depending on the phase and the element, values range between 0.1 and 0.2 electron per atom. These low electron transfers point out a covalent bonding nature, in contrast to an ionic-like interaction.

Summary

This work reports on a comprehensive structural characterization of the various allotropic forms of As_2Te_3. Nearly single-phase metastable β–As_2Te_3 was obtained following a "slow" quenching process, and its rhombohedral structure at ambient temperature was accurately redetermined and compared to those of Bi_2Te_3 and Sb_2Te_3. Its reconstructive transformation to α–As_2Te_3 at 480 K was investigated by DSC and X-ray thermo diffraction. Particular attention was given to the As atomic displacements inside the van der Waals interspace which structurally relates β–As_2Te_3 to α-As_2Te_3.

The low-temperature behavior of β–As_2Te_3 was investigated by means of transport and thermodynamic measurements. A structural transition was evidenced at 205 – 210 K, and investigated by combining X-ray and neutron thermo diffraction. The crystal structure of the new β'–As_2Te_3 phase formed is a monoclinic variant of β–As_2Te_3 exhibiting both a distortion and a 4-fold modulation along the *b*-axis. This transition very likely occurs in two steps (T_{S1} = 205 – 210 K and T_{S2} = 193 – 197 K) with modulation at T_{S1} and distortion at T_{S2}. DFT calculations provide a theoretical insight into the polymorphism of As_2Te_3. Lattice parameters, electronic band gap and heats of formation have been calculated, and agree well with the experiments. They indicate that all three structures are semiconducting. Heat of formation calculated values evidence that the α–phase is more stable than the β'–phase, which is more stable than the β–phase. Moreover, the ELF representations confirm the occurrence of a van der Waals bonding between covalently bonded As_2Te_3 layers in all three structures.

Acknowledgements

The authors acknowledge the financial support from the French National Agency (ANR) in the frame of its program “PROGELEC” (Verre Thermo-Générateur “VTG”). DFT and phonon calculations were performed using HPC resources from GENCI - CINES (Grant 2015-096175). B. Fraisse and R. Escalier are greatly acknowledged for their help in the low temperature X-Ray diffraction experiments, M. Bigot for the preparation of amorphous As_2Te_3 and M. Ceretti for valuable discussions.

Corresponding author Information:

Eric Alleno

ICMPE

UMR7182 CNRS – UPEC

2-8, rue H. Dunant

94320 THIAIS

FRANCE

Tel. +33 1 49 78 12 37

e-mail: eric.alleno@icmpe.cnrs.fr

References

(1) Nolas, G. S.; Sharp, J.; Goldsmid, H. J. In *Thermoelectrics: Basic principles and new materials developments*; Hull, R., Osgood, R. M., Sakaki, H., Zunger, A., Eds.; Springer: Berlin, 2001, p 111.

(2) Scherrer, H.; Scherrer, S. In *CRC handbook of thermoelectrics*; Rowe, D. M., Ed.; CRC Press: Boca Raton, 1995.

(3) Stordeur, M. In *CRC handbook of thermoelectrics*; Rowe, D. M., Ed.; CRC Press: Boca Raton, 1995.

(4) Vaney, J.-B.; Carreaud, J.; Delaizir, G.; Pradel, A.; Piarristeguy, A.; Morin, C.; Alleno, E.; Monnier, J.; Gonçalves, A. P.; Candolfi, C.; Dauscher, A.; Lenoir, B. *Advanced Electronic Materials* **2015**, n/a. , DOI: 10.1002/aelm.201400008.

(5) Shu, H. W.; Jaulmes, S.; Flahaut, J. *Mater. Res. Bull.* **1986**, *21*, 1509-1514.

(6) Kanishcheva, A. S.; Milhailov, Y. N.; Chernov, A. P. *Inorg. Mater.* **1982**, *18*, 796-799.

(7) Stergiou, A. C.; Rentzeperis, P. J. *Z. Kristallogr.* **1985**, *172*, 139-145.

(8) Cornet, J.; Rossier, D. *J. Non-Cryst. Solids* **1973**, *12*, 61-84.

(9) Toscani, S.; Dugue, J.; Ollitrault, R.; Ceolin, R. *Thermochim. Acta* **1991**, *186*, 247-251.

(10) Hsieh, D.; Xia, Y.; Qian, D.; Wray, L.; Meier, F.; Dil, J. H.; Osterwalder, J.; Patthey, L.; Fedorov, A. V.; Lin, H.; Bansil, A.; Grauer, D.; Hor, Y. S.; Cava, R. J.; Hasan, M. Z. *Phys. Rev. Lett.* **2009**, *103*, 146401.

(11) Xia, Y.; Qian, D.; Hsieh, D.; Wray, L.; Pal, A.; Lin, H.; Bansil, A.; Grauer, D.; Hor, Y. S.; Cava, R. J.; Hasan, M. Z. *Nature Physics* **2009**, *5*, 398-402.

(12) Chen, Y. L.; Chu, J. H.; Analytis, J. G.; Liu, Z. K.; Igarashi, K.; Kuo, H. H.; Qi, X. L.; Mo, S. K.; Moore, R. G.; Lu, D. H.; Hashimoto, M.; Sasagawa, T.; Zhang, S. C.; Fisher, I. R.; Hussain, Z.; Shen, Z. X. *Science* **2010**, *329*, 659-662.

(13) Roushan, P.; Seo, J.; Parker, C. V.; Hor, Y. S.; Hsieh, D.; Qian, D.; Richardella, A.; Hasan, M. Z.; Cava, R. J.; Yazdani, A. *Nature* **2009**, *460*, 1106-U1164.

(14) Murakami, S. *New Journal of Physics* **2011**, *13*, 105007.

(15) Pal, K.; Waghmare, U. V. *Appl. Phys. Lett.* **2014**, *105*, 062105.

(16) Platakis, N. S. *J. Non-Cryst. Solids* **1977**, *24*, 365-376.

(17) Ho, C. H. *J. Alloys Compd.*, *509*, 7198-7204.

(18) Johnson, R. T.; Quinn, R. K.; Northrop, D. A.; Borders, J. A. *Bull. Amer. Phys. Soc.* **1971**, *16*, 839-&.

(19) Bludska, J.; Karamazov, S.; Navratil, J.; Jakubec, I.; Horak, J. *Solid State Ionics* **2004**, *171*, 251-259.

(20) Chen, C.-h.; Chen, S.-w.; Wang, J.-l. *Mater. Chem. Phys.* **2001**, *70*, 316-325.

(21) Pradel, A.; Pagnier, T.; Ribes, M. *Solid State Ionics* **1985**, *17*, 147-154.

(22) Almeida, M.; Alcacer, L.; Oostra, S. *Phys. Rev. B* **1984**, *30*, 2839-2844.

(23) Rodriguezcarvajal, J. *Physica B* **1993**, *192*, 55-69.

(24) Blöchl, P. E. *Phys. Rev. B* **1994**, *50*, 17953-17979.

(25) Kresse, G.; Hafner, J. *Phys. Rev. B* **1993**, *47*, 558-561.

(26) Kresse, G.; Furthmüller, J. *Phys. Rev. B* **1996**, *54*, 11169-11186.

(27) Perdew, J. P.; Burke, K.; Ernzerhof, M. *Phys. Rev. Lett.* **1997**, *78*, 1396.

(28) Chaput, L.; Togo, A.; Tanaka, I.; Hug, G. *Phys. Rev. B* **2011**, *84*, 094302.

(29) Parlinski, K.; Li, Z. Q.; Kawazoe, Y. *Phys. Rev. Lett.* **1997**, *78*, 4063-4066.

(30) Togo, A.; Oba, F.; Tanaka, I. *Phys. Rev. B* **2008**, *78*, 134106.

(31) Henkelman, G.; Arnaldsson, A.; Jonsson, H. *Computational Materials Science* **2006**, *36*, 354-360.

(32) Scheidemantel, T. J.; Meng, J. F.; Badding, J. V. *J. Phys. Chem. Solids* **2005**, *66*, 1744-1747.

(33) Quinn, R. K. *Mater. Res. Bull.* **1974**, *9*, 803-813.

(34) Zhao, X. J.; Yin, H. B.; Chen, W. M. *J. Non-Cryst. Solids* **1995**, *184*, 128-132.

(35) Drabble, J. R.; Goodman, C. H. L. *J. Phys. Chem. Solids* **1958**, *5*, 142-144.
(36) Björkman, T.; Gulans, A.; Krasheninnikov, A. V.; Nieminen, R. M. *Phys. Rev. Lett.* **2012**, *108*, 235502.
(37) Mukai, K.; Kishida, Y.; Nozaki, H.; Dohmae, K. *Chem. Mater.* **2013**, *25*, 2828-2837.
(38) Werner, P. E.; Eriksson, L.; Westdahl, M. *J. Appl. Crystallogr.* **1985**, *18*, 367.
(39) Dove, M. T. *American Mineralogist* **1997**, *82*, 213-244.
(40) Silvi, B.; Savin, A. **1994**, *371*, 683-686.
(41) Anderson, T. L.; Krause, H. B. *Acta Crystallographica Section B-Structural Science* **1974**, *30*, 1307-1310.
(42) Feutelais, Y.; Legendre, B.; Rodier, N.; Agafonov, V. *Mater. Res. Bull.* **1993**, *28*, 591-596.

Captions to the Tables

Table 1: Atom labels, Wyckoff position, site occupancy factor and atom coordinates for β-As_2Te_3 at 300 K.

Table 2: Selected distances and angles in β–As_2Te_3 compared to the data of Shu *et al.*[5] and to isostructural, *R-3m*, X_2Te_3 compounds (*X* = Sb or Bi).

Table 3: Atom labels, Wyckoff position, site occupancy factor and atom coordinates for α–As_2Te_3 at 300 K.

Table 4: Selected bond distances in α–As_2Te_3.

Table 5: Structural parameters for β'–As_2Te_3 at 20 K determined by Rietveld refinement of the neutron diffraction pattern.

Table 6: Averaged atomic distances in β'–As_2Te_3 compared to β–As_2Te_3. See text for explanation.

Table 7: Crystallographic parameters, electronic band gap, phonon supercell details, and heats of formation (gross and ZPE corrected) of the polymorphic As_2Te_3 phases obtained after the full DFT relaxation.

Table 8: Bader electronic charges of inequivalent As and Te atoms in the polymorphic As_2Te_3 phases. Because of the large number of inequivalent sites in the β'–phase ($P2_1/m$), the values are not given, but are similar to the corresponding sites in pseudo β'–phase $C2/m$.

Tables

Table 1

Atom	Wyckoff	Occupancy	*x*	*y*	*z*
Te1	3*a*	1	0	0	0
Te2	6*c*	1	0	0	0.2155(1)
As	6*c*	1	0	0	0.3977(1)
R-3m, a = 4.047(1) Å, *c* = 29.498(2) Å, R_B = 4.3 % and R_{wp} = 6.8 %					

Table 2

	Compound	β-As_2Te_3 (this work)	β-As_2Te_3 [5]	Sb_2Te_3 [41]	Bi_2Te_3 [42]
Distances (Å)	*X* – Te1	3.016	3.132	3.200	3.258
	X – Te2	2.806	2.745	3.004	3.066
	Te2 – Te2	3.732	3.684	3.596	3.647
	d_i	2.909	2.844	2.621	2.620
Angles (°)	Te1 – *X* - Te1	84.3	80.7	83.6	84.8
	Te2 – *X* - Te2	92.3	95.3	90.4	91.6
	Te1 – *X* - Te2	91.6	91.5	92.9	91.7
	X - Te1 - *X*	95.7	99.3	96.5	95.2
	Te2-Te2-Te2	65.7	66.8	72.7	74.1

Table 3

Atom	Wyckoff	Occupancy	*x*	*y*	*z*
Te1	4*i*	1	0.0289(1)	0.0	0.2884(1)
Te2	4*i*	1	0.2780(1)	0.5	0.3406(1)
As1	4*i*	1	0.1129(1)	0.5	0.4404(1)
Te3	4*i*	1	0.3747(1)	0.0	0.0363(1)
As2	4*i*	1	0.2010(1)	0.0	0.1408(1)
C2/m, a = 14.337(1) Å, *b* = 4.015(1) Å, *c* = 9.887(1) Å, β = 95.06°, R_B = 7.2 % and R_{wp} = 10.1 %					

Table 4

	Bond	Distances (Å)
covalent bonds	Te1 - As1	2.724
	Te1 – As2	2.975
	Te2 – As1	2.644
		3.251
	Te2 – As2	2.961
	Te3 – As2	2.779
		2.818
V. d. Waals	Te1 – Te2	3.679
	Te1 – Te3	3.763
	Te3 – Te3	3.725
	As1 – As1	3.541

Table 5

Atom	Wyckoff	Occupancy	*x*	*y*	*z*	Parentage position
Te1	2*a*	1	0	0	0.	Te1
Te2	2*e*	1	-0.0122 (19)	1/4	-0.0173 (19)	Te1
Te3	4*f*	1	0.4832 (13)	0.1233 (7)	-0.0082 (13)	Te1
Te4	4*f*	1	0.1859 (14)	0	0.6437 (14)	Te2
Te5	2*e*	1	0.1914 (18)	1/4	0.6488 (19)	Te2
Te6	2*e*	1	0.2551 (18)	3/4	0.6158 (16)	Te2
Te7	4*f*	1	0.7129 (14)	0.1245 (5)	0.6532 (11)	Te2
Te8	4*f*	1	0.7207 (14)	0.6241 (6)	0.6542 (8)	Te2
As1	2*e*	1	0.3821 (19)	1/4	0.2200 (18)	As
As2	2*e*	1	0.4291 (17)	3/4	0.1916 (17)	As
As3	4*f*	1	0.4070 (12)	-0.0208 (5)	0.1756 (11)	As
As4	4*f*	1	0.1063 (12)	0.1307 (5)	0.8236 (10)	As
As5	4*f*	1	0.0964 (15)	0.6200 (5)	0.7891 (10)	As
$P2_1/m$, a = 6.99(1) Å, b = 16.24(1) Å; c = 10.25(1) Å; β = 103.4(1)° (NPD)						
$P2_1/m$, a = 6.982(1) Å, b = 16.187(1) Å; c = 10.232(1) Å; β = 103.47(1)° (PXRD)						

Table 6

	Bond	β-As_2Te_3	β'-As_2Te_3	
			mean	range
Distances (Å)	As parentage - Te1 parentage	3.016	3.036	[2.631-3.314]
	As parentage - Te2 parentage	2.806	2.852	[2.611-3.194]
	Te2 parentage - Te2 parentage	3.734	3.780	[3.461-3.893]

Table 7

	α	β	β'	β'
	*C*2/*m* (12)	*R*-3*m* (166)	$P2_1/m$ (11)	*C*2/*m* (12)
a (Å)	14.962	4.102	7.087	7.088
b (Å)	4.071	-	16.366	4.092
c (Å)	10.130	29.745×	10.475	10.463
β	95.579	-	103.016	103.044
Volume ($Å^3$/atom)	30.701	28.893	29.592	29.560
Band gap (eV)	0.46	0.30	0.39	0.39
Phonon supercell	2×2×2 (80 at.)	2×2×1 (60 at)	1×1×1 (80 at)	2×2×2 (80 at.)
$\Delta_f H$ (kJ/mol-at)	-1.60	-0.66	-0.74	-0.74
$\Delta_f H^{cor}$ (kJ/mol-at)	-1.69	-0.88	-0.99	-1.00

Table 8

α		β		β'	
*C*2/*m* (12)		*R*-3*m* (166)		*C*2/*m* (12)	
Te1 (4*i*)	+0.10	Te1 (6*c*)	+0.08	Te1 (2*a*)	+0.18
Te2 (4*i*)	+0.09	Te2 (3*a*)	+0.15	Te2 (4*i*)	+0.09
Te3 (4*i*)	+0.11				
As1 (4*i*)	-0.11	As (6*c*)	-0.16	As (4*i*)	-0.18
As2 (4*i*)	-0.19				

Captions to the figures

Figure 1: PXRD patterns of As_2Te_3 samples obtained by crystallization at 403 K and 423 K from glassy–As_2Te_3 under 50 MPa. The blue circles and the red squares indicate the reflections of AsTe and β–As_2Te_3, respectively.

Figure 2: Experimental XRD pattern of β–As_2Te_3 at room temperature and its Rietveld analysis. The open red circles are the experimental data, the black line is the calculated pattern, the bottom blue line is the difference pattern (exp. - calc.) and the green ticks correspond to the 2θ Bragg-angles of β–As_2Te_3 (first row), AsTe (second row) and arselonith-As_2O_3 (third row), respectively.

Figure 3: SEM image in secondary electron mode of β–As_2Te_3 synthesized with a slow quenching process.

Figure 4: Sketch of the layered structure of β–As_2Te_3. As is in black, Te is in light grey, straight and dotted lines represent covalent and van der Waals bonds, respectively.

Figure 5: DSC data collected with a heating rate of 10 $K.min^{-1}$ highlighting the β–to–α transformation of As_2Te_3. The inset shows a 2D plot of the X-ray powder thermodiffraction patterns in the vicinity of the β–to–α transformation of As_2Te_3.

Figure 6: Experimental XRD pattern of α–As_2Te_3 at room temperature and its Rietveld analysis. The open red circles are the experimental data, the black line is the calculated pattern, the bottom blue line is the difference between the experimental and calculated patterns and the green ticks stand for the Bragg reflections of α–As_2Te_3.

Figure 7: Sketch of the zigzag layered structure of α–As_2Te_3 (a) and coordination of the five atomic sites (b). As is in black, Te is in light grey, straight and dotted lines represent covalent and van der Waals bonds, respectively.

Figure 8: Structural relationships between β–As_2Te_3 and α-As_2Te_3. Panel a: rhombohedral β–As_2Te_3 projected in its (2**a+b**, **c**) plane with covalently bonded As and Te layers; panel b: β-As_2Te_3 with arrows showing As displacements in the van der Waals interspace; panel c: displaced As atoms as

well as relaxed Te atoms; panel d: monoclinic α-As_2Te_3 projected in its (**a**, **c**) plane with covalently bonded As and Te zig-zag layers. As and Te atoms are in black and light grey, respectively.

Figure 9: Normalized resistance data (a) and its derivative (b) for β–As_2Te_3 at low temperature.

Figure 10: (a) Specific heat C_p of the β–As_2Te_3 compound as a function of temperature. The horizontal black line stands for the Dulong-Petit limit of 3*NR* where *N* is the number of atoms per formula unit and *R* is the gas constant. (b) DSC data measured on β–As_2Te_3 between 210 K and 150 K at 10 K·min^{-1}, blue and red colors correspond to cooling and heating part of the curve, respectively. Green dotted lines correspond to two-peak de-convolution of the DSC signal (cooling), see text for more details.

Figure 11: Neutron powder data for β-As_2Te_3 between 10° and 60° at 298K and 20K. Inset: 2D plot of the whole thermodiffraction data for β-As_2Te_3. (* AsTe, ** As_2O_3 (arselonith), *** As_2O_5; **** un-identified impurities, ▲ un-indexed modulated reflections when using a base-centered monoclinic unit cell with a = 6.984 Å, b = 4.049 Å, c = 10.238 Å, β = 103.45°).

Figure 12: Experimental PXRD pattern of β'–As_2Te_3 at 20 K and its Rietveld analysis. The open red circles are the experimental data, the black line is the calculated pattern, the bottom blue line is the difference and the green ticks stand for the Bragg reflections of β–As_2Te_3 (first row), AsTe (second row) and arselonith-As_2O_3 (third row). The inset shows a magnification of the (0 1 5), (0 1 11) and (0 2 10) lines (rhombohedral settings) at 300 K and 20 K (in red and blue, respectively) to highlight their splitting arising from the monoclinic distortion upon cooling.

Figure 13: Experimental neutron pattern for β'–As_2Te_3 at 20 K and its Rietveld analyses. The open red circles are the experimental data, the black line is the calculated pattern, the bottom blue line is the difference and the green ticks stand for the Bragg reflections of β'–As_2Te_3 (first row) and secondary phases AsTe (second row), arselonith As_2O_3 (third row), As_2O_5 (fourth row). The fit to the weak intensity lines in the low angle region can be seen in the inset.

Figure 14: Sketch of the β'–As_2Te_3 structure extending over a unit cell with two additional Te atoms.

Figure 15 : Neutron powder thermodiffraction data between 10° and 60° as a function of temperature (cooling) for β–As_2Te_3.

Figure 16: Variations with temperature of the distortion parameters $\Delta\alpha$ and $\Delta\beta$, derived from Rietveld refinements of NPD patterns.

Figure 17: Representation of the DFT-relaxed structures of the As_2Te_3 compound in its three possible polymorphic phases. As and Te atoms are represented by black and white spheres, respectively. Bond sticks symbolize pair-distances below 3.5 Å. Selected plans have been chosen to show the electronic localization function (ELF).

Figure 1

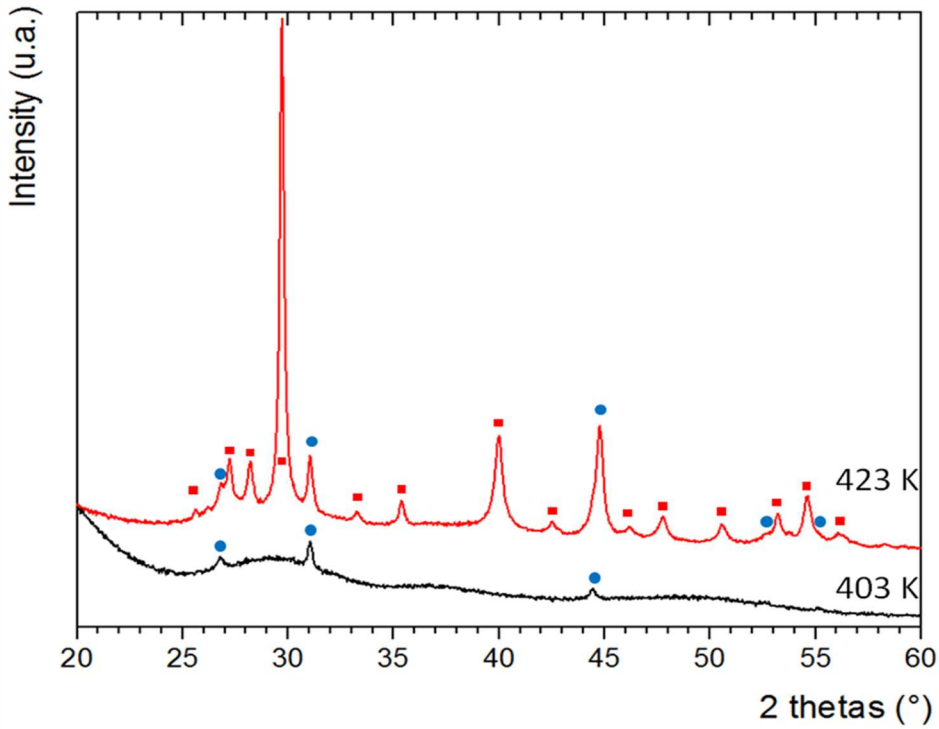

Figure 2

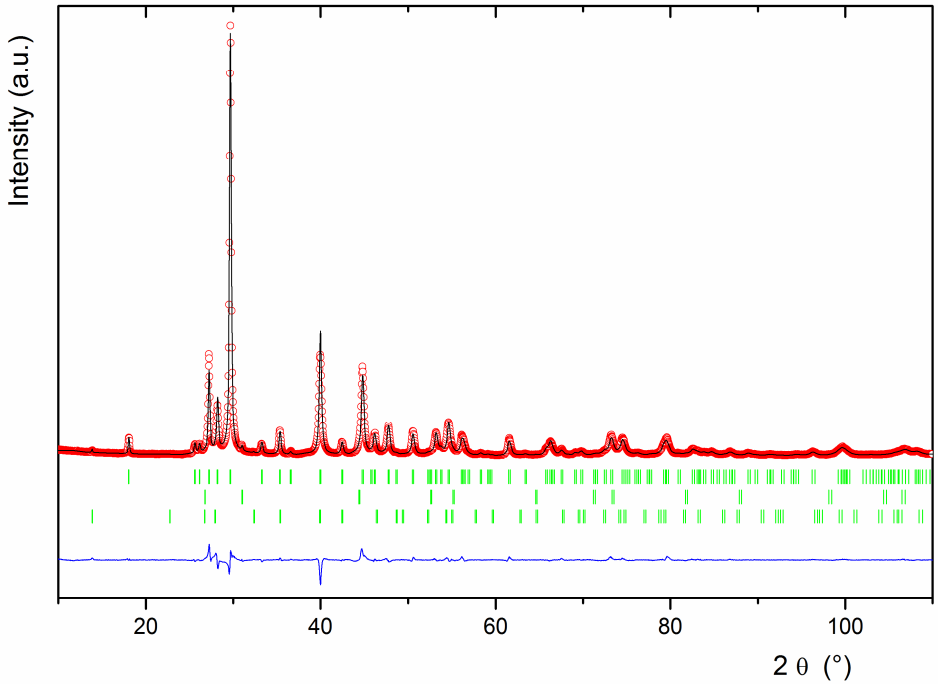

Figure 3

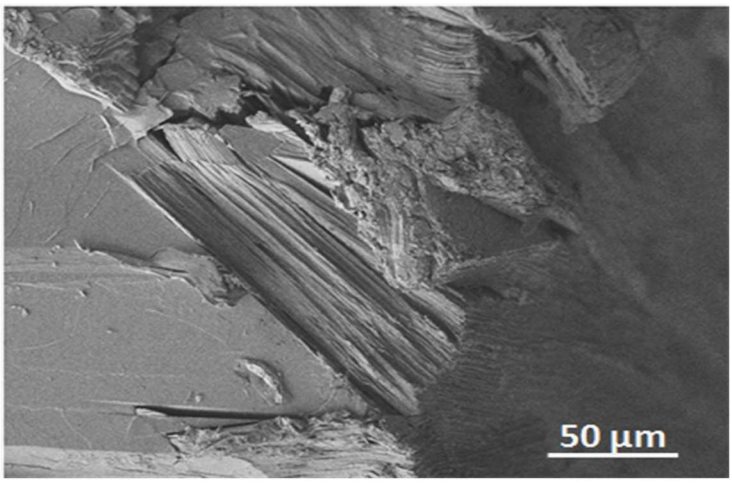

Figure 4

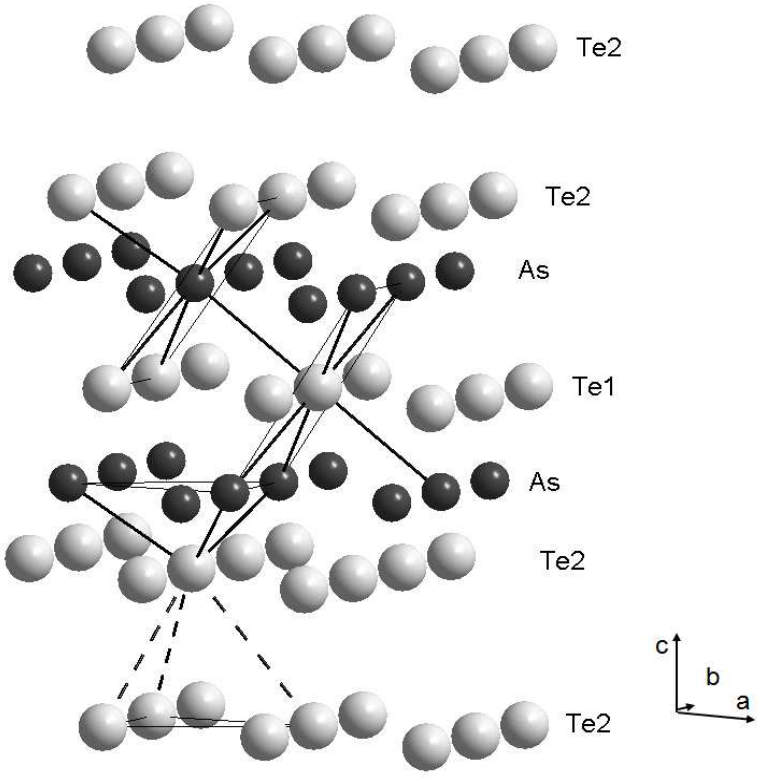

Figure 5

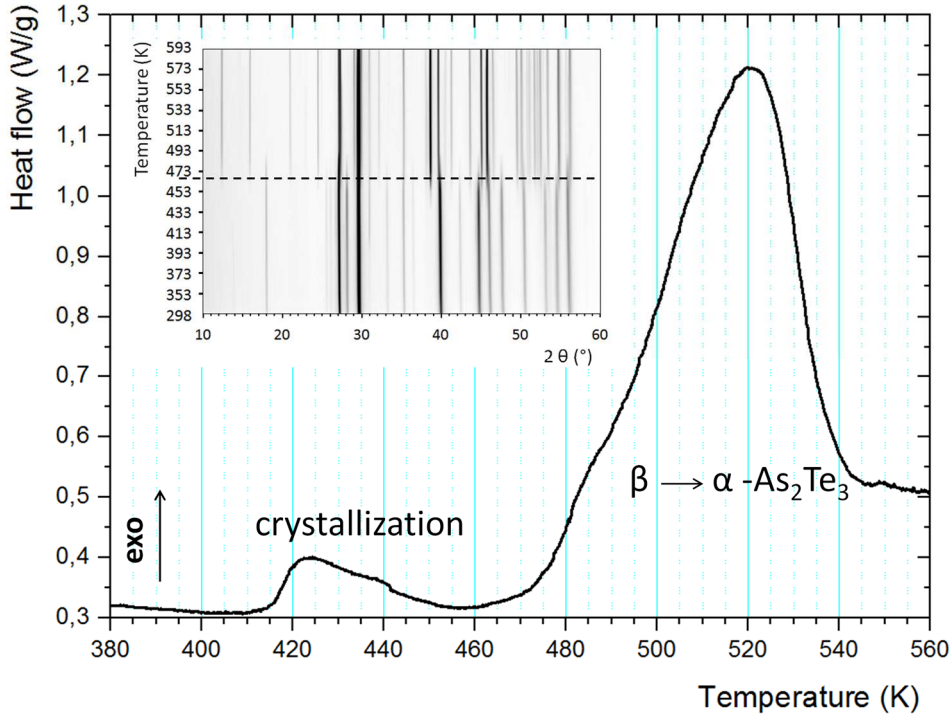

Figure 6

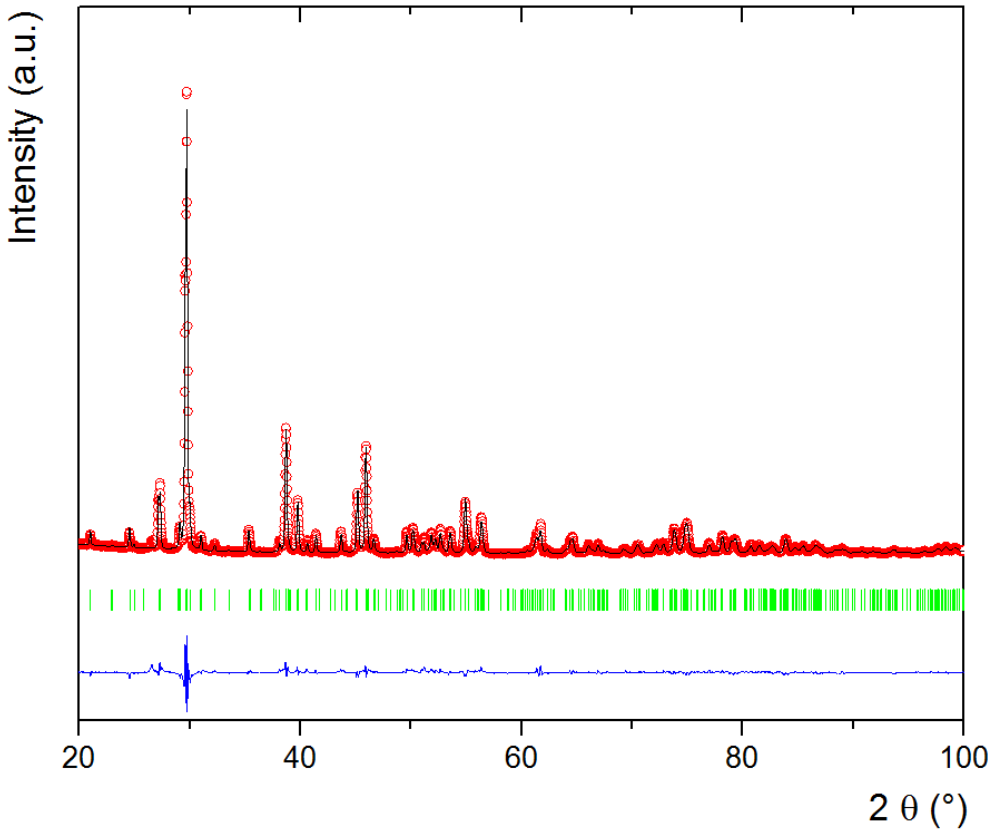

Figure 7

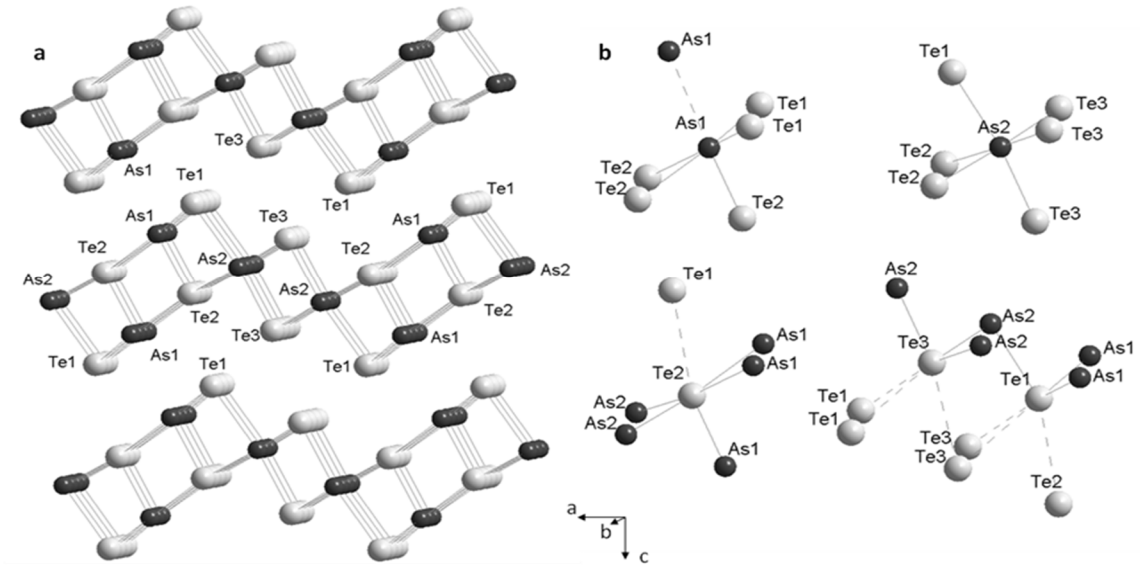

Figure 8

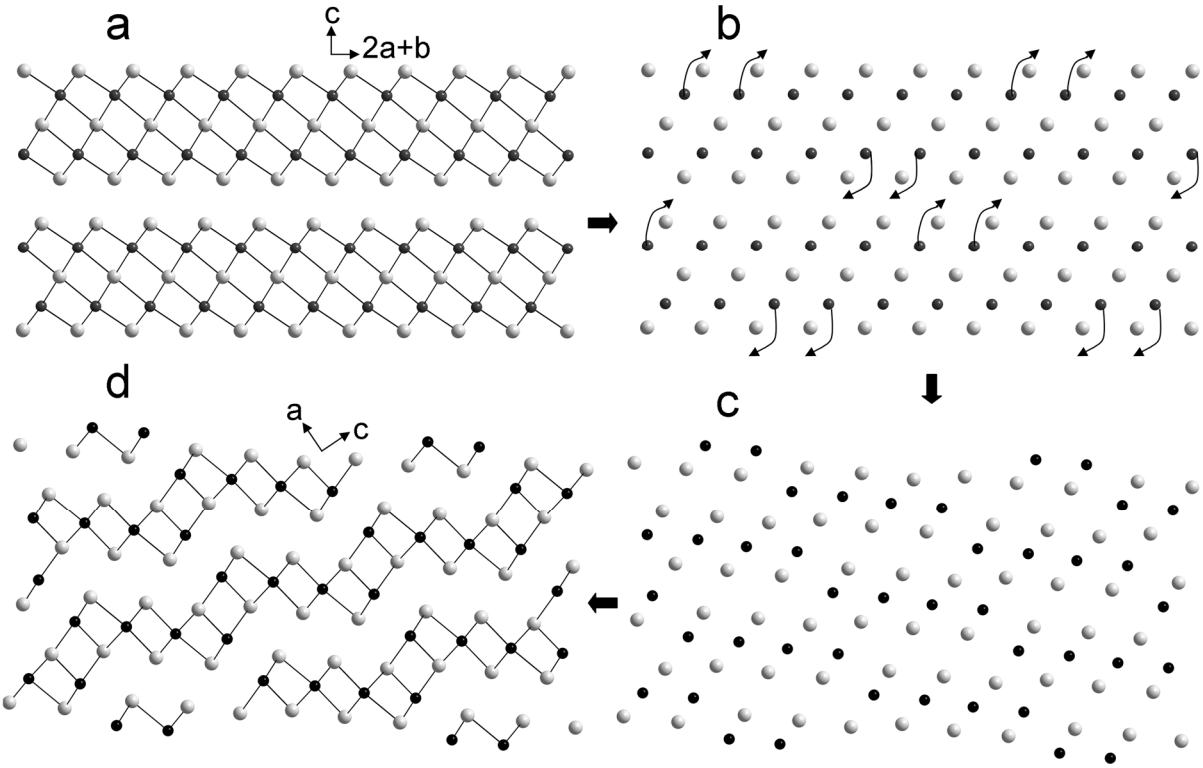

Figure 9

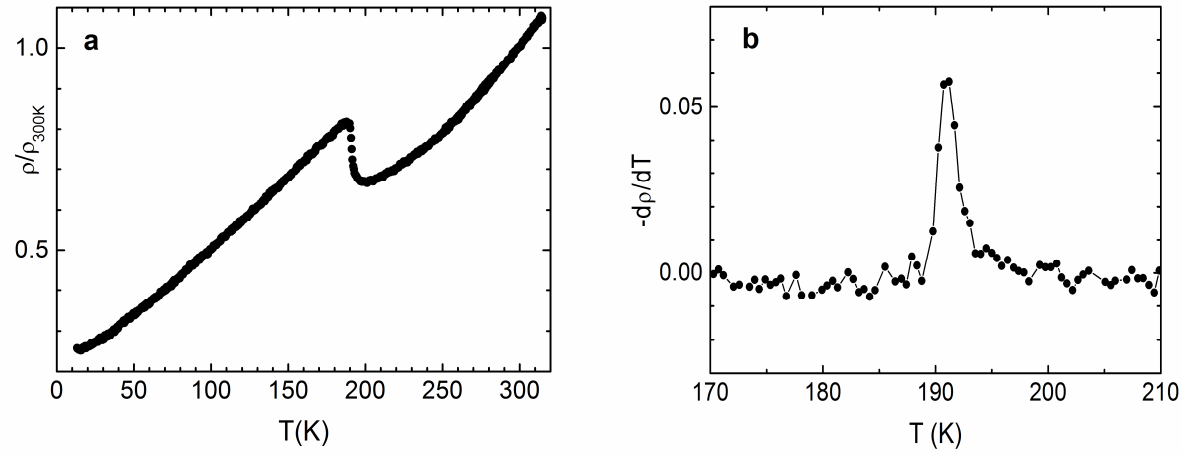

Figure 10

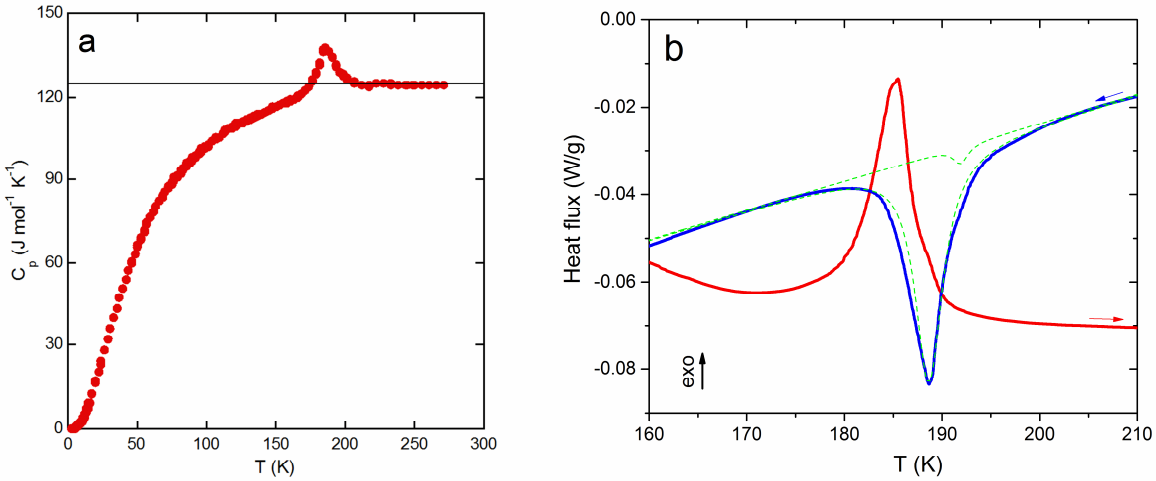

Figure 11

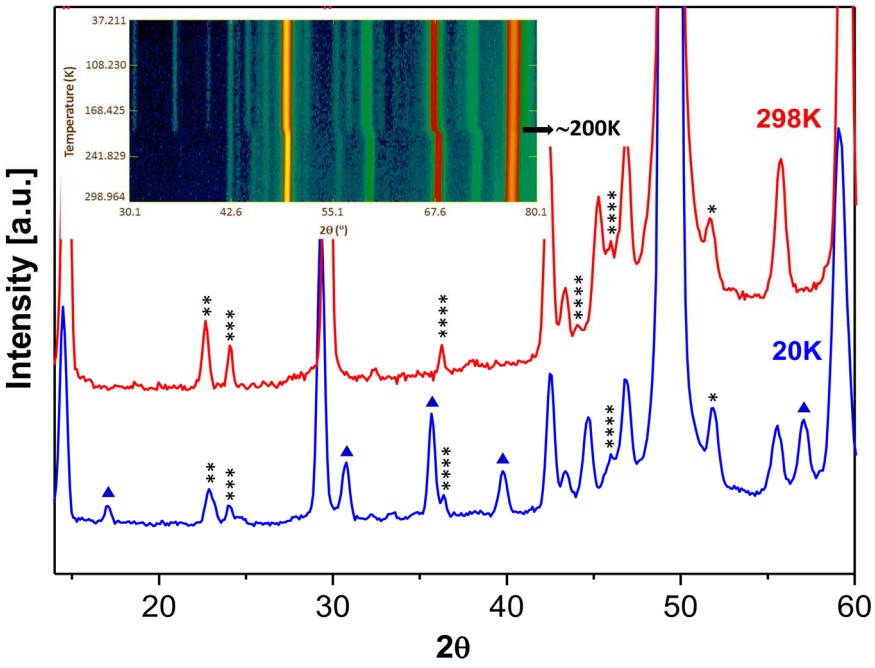

Figure 12

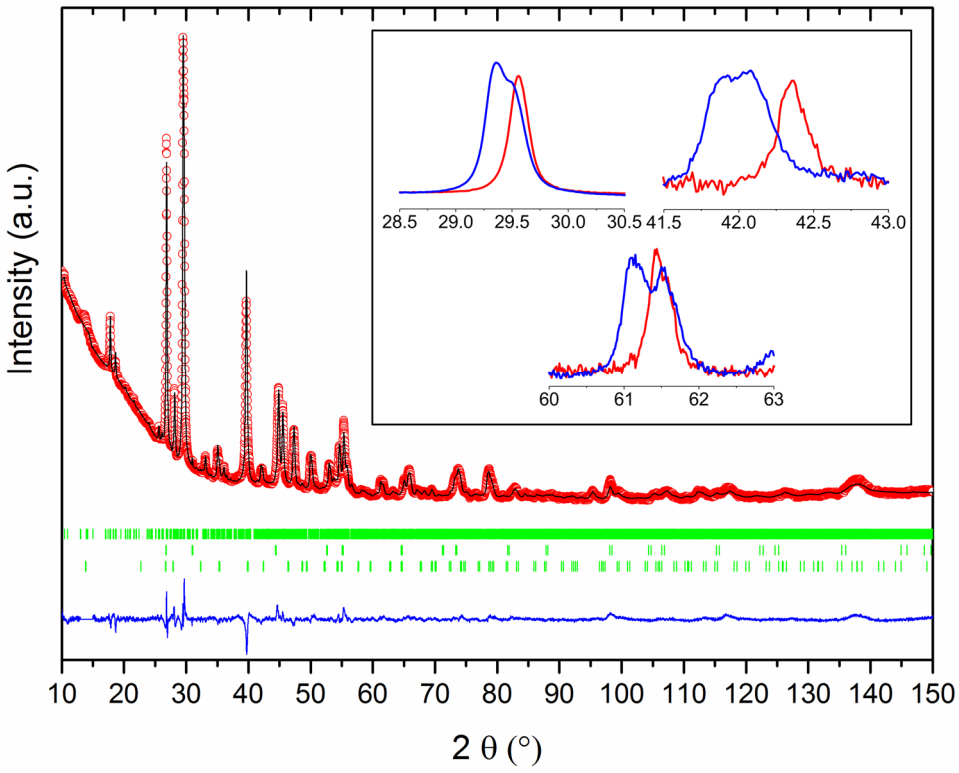

Figure 13

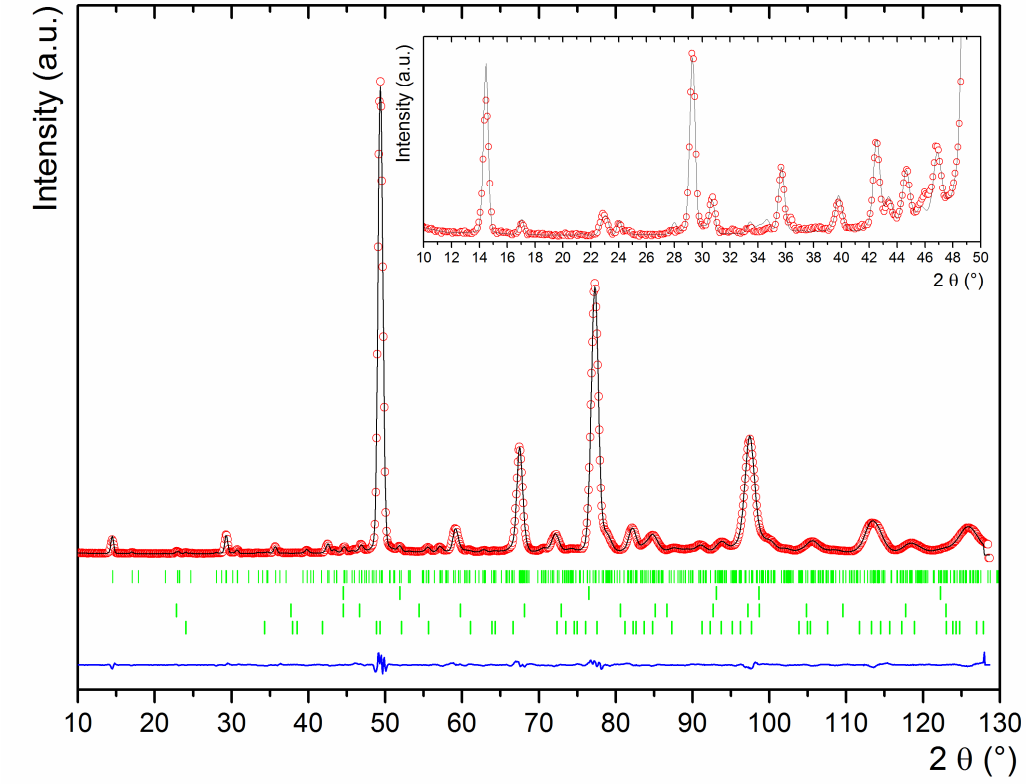

Figure 14

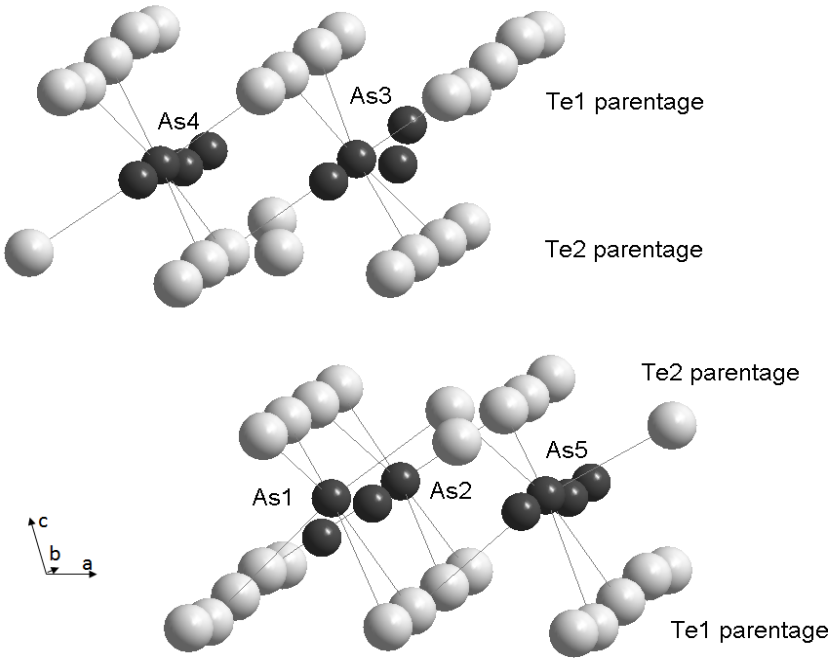

Figure 15

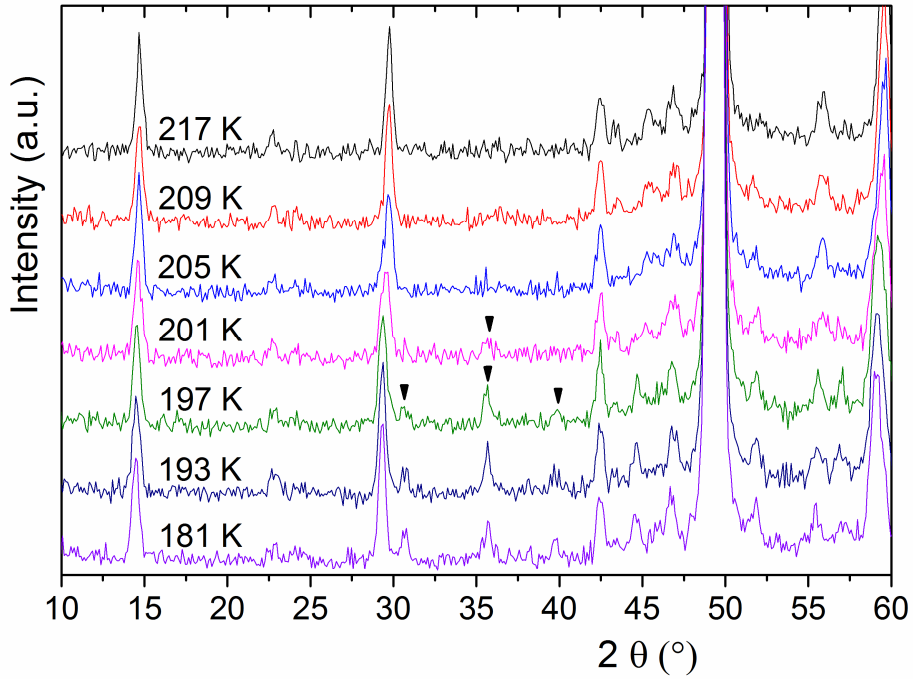

Figure 16

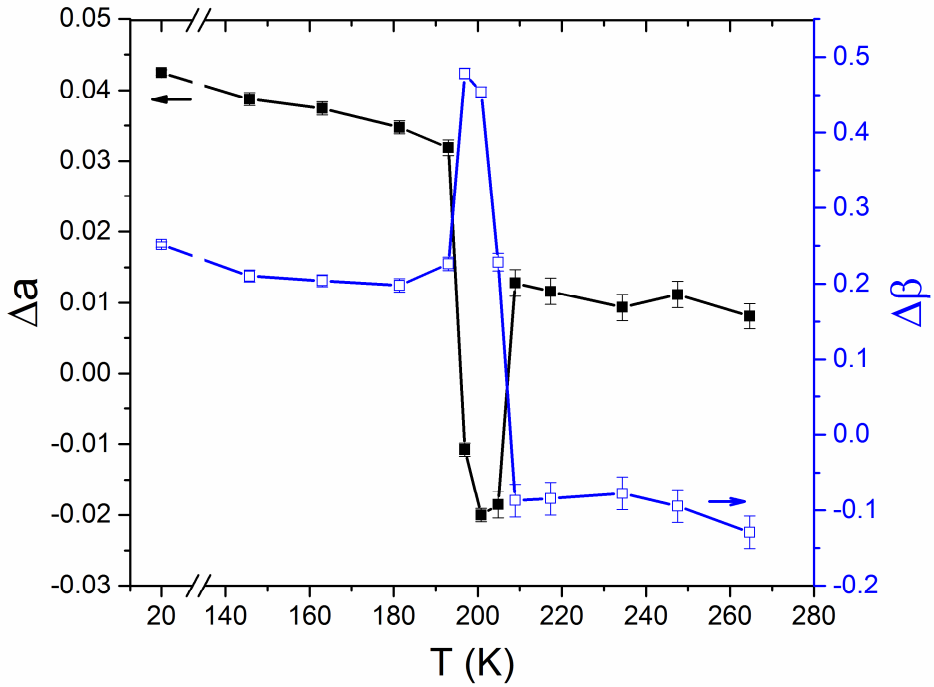

Figure 17

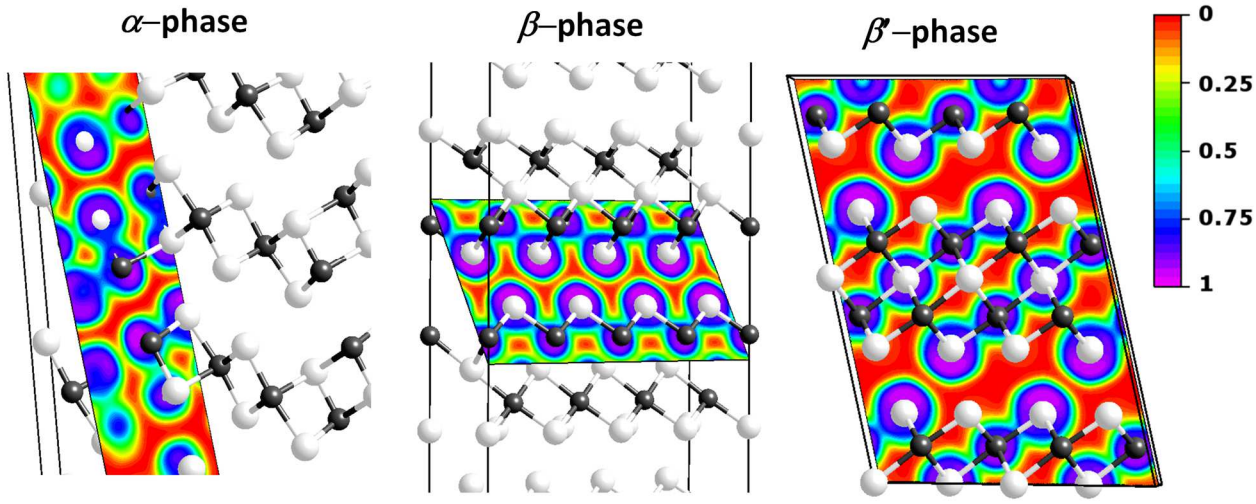

For Table of Contents Only

At 300K, As_2Te_3 can crystallize in the stable α–As_2Te_3 structure and in the metastable β–As_2Te_3 structure. Upon cooling, β–As_2Te_3 (rhombohedral) undergoes a structural transition to a new β'–As_2Te_3 allotrope (monoclinic) between 190 – 200 K. This displacive transition gives rise to an anomaly in the electrical resistance as a function of temperature.